https://doi.org/10.1016/j.electacta.2019.04.126

Exploring oxygen electrocatalytic activity and pseudocapacitive behavior of Co_3O_4 nanoplates in alkaline solutions

Peng Tan[1,2], Zhen Wu[2,3], Bin Chen[2,4], Haoran Xu[2], Weizi Cai[2], Wei He[2], Meng Ni[2,5,*]

1 Department of Thermal Science and Energy Engineering, University of Science and Technology of China, Hefei 230026, Anhui, China
2 Department of Building and Real Estate, The Hong Kong Polytechnic University, Hung Hom, Kowloon, Hong Kong, China
3 Shaanxi Key Laboratory of Energy Chemical Process Intensification, School of Chemical Engineering and Technology, Xi'an Jiaotong University, Xi'an 710049, Shaanxi, China
4 Institute of Deep Earth Sciences and Green Energy, Shenzhen University, Shenzhen 518060, China
5 Environmental Energy Research Group, Research Institute for Sustainable Urban Development (RISUD), The Hong Kong Polytechnic University, Hung Hom, Kowloon, Hong Kong, China

*Corresponding Author, Tel: +852-27664152, E-mail: meng.ni@polyu.edu.hk (Meng Ni)

Abstract: Cobalt-based materials are regarded as important materials for oxygen reduction and evolution reactions (ORR and OER) in metal-air batteries and supercapacitors. However, the activity of oxygen electrocatalysis and the pseudocapacitive performance of cobalt oxide (Co_3O_4) in the reported works are usually inconsistent. To explore this issue, a series of Co_3O_4 nanoplates are fabricated using different calcination temperatures, and their morphologies, microstructures, and electrochemical behaviors in alkaline solutions are systemically characterized. It is found that the high calcination temperature destroys the hexagonal nanoplate morphology and leads to decreased surface areas and pore volumes. In addition, the activity of Co_3O_4 nanoplates toward the ORR and OER and the capacitance values decrease with an increase of the calcination temperature. From the ORR/OER activity and specific capacitance normalized by the specific and electrochemical surface area, the intrinsic electrochemical performance may be correlated to

the surface oxidation states of Co and O. The high calcination temperature leads to the high amounts of adsorbed oxygen species and Co^{3+} atoms on the surface, which may be the key for the high intrinsic ORR and OER activity based on the electrochemical surface area. However, the apparent performance is insufficient due to the greatly reduced surface area. For the pseudocapacitive performance, on the contrary, the greater amount of Co^{2+} on the surface is favorable. Hence, the inconsistent electrochemical performance of Co_3O_4 may originate from different geometries and surface oxidation states on the surface, which are affected by the calcination temperatures in the synthesis process. This work provides insights into the design and optimization of non-precious materials in electrochemical systems, and offers a feasible strategy to improve the performance by using a low-temperature calcination method.

Keywords: cobalt oxide; calcination temperature; oxygen electrocatalysis; pseudocapacitive behavior

1. Introduction

The advancement in electrochemical energy storage systems requires low-cost and efficient power sources [1]. Although lithium-ion batteries have been widely used in various applications, the investigations on other energy conversion and storage systems are in urgent demand, such as metal-air batteries, fuel cells, and supercapacitors. Among them, metal-air batteries have attracted great attention [2–5]. They use metal directly (e.g., Li, Na, Zn) as one electrode, which has a high theoretical capacity [6]; and the other reactant, oxygen, is absorbed from the air rather than occupying the mass and volume of the battery, enhancing the energy density [7,8]. Their working mechanisms during discharge and charge involve the dissolution and deposition of metal on the negative (metal) electrode and the oxygen reduction and evolution reactions (ORR and OER) on the positive (air) electrode [9]. However, one of the key obstacles for the

commercialization is the sluggish ORR/OER kinetics, which results in large overpotentials during discharge and charge and induces corrosions when the charge potentials are high [10]. Consequently, the battery exhibits limited energy density, low energy efficiency, and poor cycling life. Although Pt and Ir are recognized as the best electrocatalysts for the ORR and OER, respectively, the insufficient stability and high price, unfortunately, impede their wide application [11]. Therefore, the development of bifunctional catalysts with high ORR/OER activity, high stability, and low cost is essential for metal-air batteries [12].

Transition metal-based materials have been investigated for a long time [13–18], among which cobalt-based materials are regarded as important catalysts for oxygen electrocatalysis [19–23]. Even though nanostructured engineering strategies such as element-doping and carbon-compositing have been applied to enhance the electrochemical properties of cobalt-based catalysts [24–26], cobalt oxide (Co_3O_4) is still the most common materials used in metal-air batteries due to its good performance [27–30]. However, after careful examinations of the reported works, inconsistent results focusing on the electrochemical performance of Co_3O_4 in alkaline solutions have been found in two aspects. The first one is that concerning the ORR and OER activity, the performance between Co_3O_4 and another cobalt-based catalyst $Co(OH)_2$ is controversial. For example, Zhou et al. found that the ultrathin porous Co_3O_4 nanoplates calcined at 250 ^oC exhibited better OER performance than the pristine $Co(OH)_2$ nanoplates [31]. However, an entirely contrary conclusion was reported by Lee et al., in which $Co(OH)_2$ hexagonal nanoplates show even greater activity in both ORR and OER than Co_3O_4 that calcined at 400 ^oC [32]. Zong et al. found that although the mesoporous Co_3O_4 nanosheets have higher ORR and OER activity than $Co(OH)_2$ nanosheets when normalized by the geometric surface area, the conclusion is reversed when normalized by the electrochemically active surface area [33]. The

second aspect is the pseudocapacitive performance of Co_3O_4. Specifically, Wu et al. electrodeposited ultrathin porous Co_3O_4 nanosheets on Ni foam and found the redox peaks related to the redox reactions for OH^- ions with Co_3O_4 [34,35]. Based on the high pseudocapacitance of Co_3O_4, a Zn-Co_3O_4 battery was built and exhibited a high voltage of 1.78 V, an energy density of 241 Wh kg^{-1}, and capacity retention ratio of 80% after 2000 cycles [36]. Through utilizing the activity toward oxygen reactions and the pseudocapacitive behavior of Co_3O_4, a hybrid Zn battery combining Zn-Co_3O_4 and Zn-air batteries was developed in our previous work, which delivered a discharge voltage of 1.85 V, a capacity of 792 mAh g_{Zn}^{-1}, and remarkable cycling stability with high energy efficiency [37–39]. However, using a similar material composed of Co_3O_4 nanosheets on carbon cloth, a rechargeable Zn-air battery showed solely the ORR and OER processes without pseudocapacitive behaviors [33]. Besides Co_3O_4 nanosheets, Co_3O_4 nanowire array grown onto the stainless steel mesh was applied in Zn-air batteries, but only voltage plateaus corresponding to the ORR and OER were exhibited and no pseudocapacitance was ever demonstrated [40].

From the above discussion, the inconsistent results make it hard to select suitable cobalt-based catalysts for electrochemical systems and hinder the rational design of novel transition-metal-based materials. Therefore, this work aims at exploring the oxygen electrocatalytic activity and pseudocapacitive behavior of Co_3O_4 in alkaline solutions to clarify the inconsistent results. We first fabricated $Co(OH)_2$ nanoplates using a hydrothermal reaction and then converted them to Co_3O_4 nanoplates using different calcination temperatures [41]. Their compositions, morphologies, and microstructures were characterized in detail. Then, the ORR and OER activity and the pseudocapacitive performance of $Co(OH)_2$ and Co_3O_4 nanoplates in alkaline solutions were examined. Moreover, the oxidation states of Co and O on the surface of Co_3O_4 was

analyzed from X-ray photoelectron spectroscopy. The relationship between the electrochemical performance, the geometrical properties, and the oxidation states on the surface was further discussed.

2. Experimental

2.1 Fabrication of $Co(OH)_2$ and Co_3O_4 nanoplates

$Co(OH)_2$ nanoplates were synthesized using a reported approach [42,43]. First, 0.16 mol of KOH was dissolved in 35 mL of distilled water to form a KOH solution. Then, 5 mL of 4.0 M $Co(NO_3)_2 \cdot 6H_2O$ aqueous solution was slowly dropped into it within 5 min. After continuous stirring for 30 min, the suspension was transferred into a Teflon-lined autoclave, which was heated at 100 ^oC for 12 h. After cooling naturally, the precipitate was washed thoroughly and dried at 60 ^oC overnight. The obtained powder was sintered in air at a given temperature (from 150 to 750 ^oC) for 3 hours with a heating rate of 2 $^oC\ min^{-1}$.

2.2 Physicochemical characterization

The morphologies of $Co(OH)_2$ and Co_3O_4 nanoplates were observed by a transmission electron microscope (TEM, JEOL 2100F). The compositions were examined by X-ray diffraction (XRD, Rigaku Smartlab) using a Cu-Kα source at 45 keV. The X-ray photoelectron spectroscopy (XPS) spectra were measured by PHI 5600 multi-technique system. The thermogravimetric analysis (TGA) of $Co(OH)_2$ nanoplates was conducted in the air atmosphere from 100 to 800 ^oC at a heating rate of 10 $^oC\ min^{-1}$. The nitrogen adsorption/desorption isotherms were measured on ASAP 2020. The specific surface areas were calculated by the Brunaure-Emmert-Teller (BET) method, and pore volumes and sizes were estimated from the desorption isotherms using the Barrett-Joyner-Halenda (BJH) method.

2.3 Electrochemical characterization

The electrochemical properties were characterized in a three-electrode cell by a Solartron SI 1287 potentiostat. To prepare the ink solution, 4 mg of prepared nanoplates or commercial Pt/C and Ir/C catalysts, 2 mg of Vulcan carbon (XC-72), and 20 μL of Nafion solution (5 wt%) were mixed into 380 μL of isopropanol, and then ultrasonicated for 30 minutes. After that, 4 μL of the homogeneous ink was carefully dripped onto a polished glassy carbon electrode (diameter: 5 mm, surface area: 0.2 cm^2) with a loading of 0.2 mg cm^{-2}, and dried completely as the working electrode. A graphite wire and a Hg/HgO electrode were applied as the counter and reference electrodes, respectively.

To test the ORR activity, the electrolyte (0.1 M KOH) was first saturated by oxygen. Linear sweep voltammetry (LSV) was conducted at 5 mV s^{-1} within the potential from 0.2 to −0.6 V (vs. Hg/HgO) using the rotation speeds ranging from 400 to 2500 rpm. The Koutecky-Levich equation was used to get the number of electrons transferred (*n*):

$$j^{-1} = j_k^{-1} + (0.2nFD_{O_2}^{2/3}\nu^{-1/6}C_{O_2}\omega^{1/2})^{-1} \quad (1)$$

where *j* and j_k are the measured and kinetic current densities, respective, *F* is the Faraday constant, D_{O_2} is the diffusion coefficient of O_2 (1.86×10^{-5} cm^2 s^{-1}), ν is the kinetic viscosity (1.01×10^{-2} cm^2 s^{-1}), C_{O_2} is the bulk concentration of O_2 (1.21×10^{-6} mol cm^{-3}), and ω is the rotation speed (rpm).

The OER activity was tested in a 1.0 M KOH aqueous solution. LSV for OER polarization was at 5 mV s^{-1} within the potential from 0.2 to 0.7 V (vs. Hg/HgO) using the rotation speed of 1600 rpm. Cyclic voltammetry (CV) was measured from 0.2 to 0.7 V (vs. Hg/HgO) at various scan rates, and the measured currents were normalized by the catalyst loading. The following equation was used to calculate the specific capacitance value (*C*) [44]:

$$C = \frac{1}{msΔV}\int IdV \quad (2)$$

where m is the mass loading of the active material, s is the scan rate, ΔV is the potential range, and I is the corresponding current density. The double-layer capacitance (C_{DL}) formed at the electrode/electrolyte interface was determined by carrying out the CV scans in the nonreactive potential window at the scan rate from 10 to 60 mV s^{-1}. By plotting the difference in the cathodic and anodic current densities versus the scan rates, the C_{DL} value was calculated from the slope [45]. All potentials were eventually calibrated to a reversible hydrogen electrode (RHE) scale.

3. Results and discussion

3.1 Characterization of $Co(OH)_2$ and Co_3O_4 nanoplates

Figure 1a displays the TEM image of the synthesized $Co(OH)_2$, from which an approximate hexagonal plate morphology with the length from 100 to 150 nm is presented, similar as previously reported [31]. The selected area electron diffraction (SAED) pattern (Figure 1a inset) demonstrates its polycrystalline nature. From the high-resolution image in Figure 1b, the nanoplate was composed of nanoparticles. When examining the porous structure, a typical type IV isotherm is presented in Figure 1c, and the measured specific surface area is 61.65 m^2 g^{-1}. Figure 1c inset shows the pore width distribution, and it is found that most pores are distributed within the range of 2–10 nm with an average value of 3.3 nm. The XRD pattern in Figure 1d indicates that all diffraction peaks are well indexed to β-$Co(OH)_2$ (JCPDS #74-1057) [46]. From the TGA curve of $Co(OH)_2$ nanoplates in Figure S1, we selected different annealing temperatures from 150 to 750 ^oC to treat $Co(OH)_2$ [46,47], and the results are presented in following sections.

The TEM images of the nanoplates calcined at various temperatures are presented in Figure 2, and the XRD patterns are presented in Figure 3. At the temperature of 150 ^oC, the nanoplates

maintain the hexagonal plate morphology, but the porous structure becomes more obvious when compared to the pristine $Co(OH)_2$ nanoplates (Figure 2a). The XRD result indicates that at this calcination temperature, the nanoplates are a combination of $Co(OH)_2$ and CoO(OH) (JCPDS #26-1107), which caused by the partial oxidation at the low temperature. When the calcination temperature is 200 ^oC, the porous structure composed of nanoparticles is clearly observed (Figure 2b), and no peaks corresponding to $Co(OH)_2$ or CoOOH can be detected. Instead, the peaks are indexed to the spinel Co_3O_4 (JCPDS #42-1467), indicating the that $Co(OH)_2$ was completely converted into Co_3O_4. The similar finding has been reported by Tong et al, in which $Co(OH)_2$ was decomposed to Co_3O_4 at 200 ^oC [48]. To further confirm the formation of Co_3O_4, the high-resolution TEM image shows the lattice fringes of 0.14 and 0.28 nm (Figure S2a), which correspond to the (440) and (220) planes of Co_3O_4, respectively. The SAED pattern in Figure S2b also coincides with the diffraction of Co_3O_4. At a higher calcination temperature of 250 ^oC, as shown in Figure 2c, the pores formed during the calcination process become more clear, and the diffraction peaks corresponding to Co_3O_4 become taller. When increasing the calcination temperature to 350 ^oC, the pores in the nanoplate become larger, and in some nanoplates the edges blurred (Figure 2d). From the XRD pattern in Figure 3, the diffraction peaks become much taller and narrower. Hence, the higher temperature improves the crystallinity of the nanoplates. Previous research has indicated that the near hexagonal shape of Co_3O_4 nanoplates can be well preserved at a calcination temperature below 500 ^oC, but collapsed when the temperature was above 600 ^oC. We further increased the calcination temperature to 550 ^oC, as shown in Figure 2e, the hexagonal shape is hardly observed. It is also interesting to find that the porous structure with many visible pores disappeared; instead, large pores with the diameters higher than 20 nm are presented. The similar observation has been reported by Qiu et

al. in which $Co(OH)_2$ nanosheets could be converted into Co_3O_4 nanorings by calcination in air at 600 ^oC [49]. At an even higher calcination temperature of 750 ^oC, the resultant products do not present the nanoplate morphology but become dense particles, as illustrated in Figure 2f. In addition, the particle size increases, which may be caused by the fusion of small nanoparticles at such a high temperature [12]. The XRD patterns in Figure 3 show that the diffraction peaks became much taller when the calcination temperature further increased, indicating the improved crystallinities of the Co_3O_4 nanoplates. Hence, starting from the calcination temperature of 200 ^oC, $Co(OH)_2$ nanoplates were converted to Co_3O_4. We denoted the resultant products as Co_3O_4-*x* where *x* represents the calcination temperature, and their properties are further investigated.

The nitrogen adsorption-desorption isotherms of the as-prepared Co_3O_4 nanoplates are shown in Figure 4. For Co_3O_4 nanoplates calcined at the temperature from 200 to 350 ^oC, the nitrogen adsorption-desorption isotherms can be categorized as type II with obvious type H3 hysteresis loops. With an increase of the calcination temperature, the hysteresis loops gradually disappear. The BET surface areas are calculated to be 101.15, 90.25, 83.71, 76.01, and 71.72 m^2 g^{-1} for the Co_3O_4 nanoplates calcined at 200, 250, 350, 550, and 750 ^oC, respectively. Hence, compared to that of $Co(OH)_2$ nanoplates, the surface area of Co_3O_4 nanoplates is larger, but it decreases with an increase of the calcination temperature [31]. The corresponding pore volumes and sizes are shown in Figure S3. Most pores are within the range of 2 to 10 nm for all Co_3O_4 nanoplates. For Co_3O_4 nanoplates calcined at 200 ^oC, the pore size distribution exhibits a narrow peak at 3.1 nm, indicating the uniform pore size. When the calcination temperature increases, the peak becomes wider, which means the non-uniformity of pore sizes increased. The pore volumes of Co_3O_4 nanoplates calcined at 200, 250, 300, 350, 550, and 750 ^oC are 0.409, 0.378, 0.353, 0.177, and 0.141 cm^3 g^{-1}, respectively. Hence, a higher calcination temperature leads to a lower

specific surface area and smaller pore volume, which is consistent with our TEM observations and previous investigations [42]. These differences in Co_3O_4 nanoplates calcined at different temperatures will result in different electrochemical properties.

3.2 Electrochemical activity for oxygen electrocatalysis

The ORR activity of $Co(OH)_2$ and Co_3O_4 nanoplates in the O_2-saturated 0.1 M KOH solution is presented in Figure 5a and 5b. $Co(OH)_2$ nanoplates exhibit a Tafel slope of 143.1 mV dec^{-1}, and a limiting current density of 4.78 mA cm^{-2}. For Co_3O_4 nanoplates, at the calcination temperature of 200 °C, the Tafel slope is reduced to 108.1 mV dec^{-1}, and the sample presents an enhanced limiting current density of 5.32 mA cm^{-2}. This value is high among reported Co-based nanoplate catalysts (Table S1) [32,41], and also close to that of commercial 20% Pt/C catalyst (Figure S4a). It is also interesting to find that for the transition state of the sample that is calcined at 150 °C, the ORR activity is between that of $Co(OH)_2$ and Co_3O_4 (Figure S4b). With an increase of the calcination temperature, the Tafel slope gradually increases (Figure 5b), and the limiting current density decreases (Figure 5c). Especially, the Co_3O_4 nanoplates calcined at 550 °C exhibits a similar Tafel slope to that of $Co(OH)_2$ nanoplates, and the limiting current density of the Co_3O_4 nanoplates calcined at 750 °C is even lower than that of $Co(OH)_2$ nanoplates. Thus, the activity of Co_3O_4 nanoplates toward the ORR is correlated to the calcination temperature and decreases with an increase of the calcination temperature. The LSV curves of $Co(OH)_2$ and Co_3O_4 nanoplates at different rotating rates are shown in Figure S5, and the corresponding Koutecky-Levich plots are shown inset. In Lee's work, $Co(OH)_2$ has a four-electron pathway (~3.3) but CoO and Co_3O_4 have a two-electron pathway (2.6−2.7) for the ORR [32]. In our case, the number of electrons transferred for $Co(OH)_2$ nanoplates is around 3.6, while those for Co_3O_4 nanoplates calcined at 200 to 350 °C are all close to 4.0. Even for Co_3O_4 calcined at a high

temperature of 750 °C, the number is also ~3.2 (Table S2). The result indicates that all samples may have a four-electron process. The stability of Co_3O_4 nanoplates calcined at 200 °C is tested through maintaining the potential of 0.3 V (vs. RHE) for 5 h. As shown in Figure S6a, 87.7% of the initial current can be preserved. After the stability test, we also used TEM to characterize the nanoplates. From the TEM image in Figure S6b, the hexagonal nanoplate morphology is well maintained, demonstrating the remarkable ORR stability.

The OER activity of $Co(OH)_2$ and Co_3O_4 nanoplates was investigated in 1.0 M KOH solution. Figure 5d shows that $Co(OH)_2$ nanoplates deliver a Tafel slope of 58.0 mV dec^{-1} (Figure 5e) and an overpotential of 366.8 mV at the current density of 10 mA cm^{-2}. This overpotential is only of 60 mV higher than that of Ir/C (Figure S7a) and even lower than that of the reported RuO_2 catalyst (370 mV) [50], demonstrating the high OER activity. When the calcination temperature is 150 °C, as shown in Figure S7b, different from the behaviors in the ORR performance, the OER activity of the transition state decreases. When $Co(OH)_2$ is fully converted to Co_3O_4 (200 °C), the OER activity further reduced. This result agrees well with the previous study that $Co(OH)_2$ has higher OER activity than Co_3O_4 [32]. Comparatively, the Co_3O_4 nanoplates exhibit the Tafel slopes of around ~55 mV dec^{-1}, but the overpotential at 10 mA cm^{-2} increases with the calcination temperature, as listed in Table 1. Hence, it can be concluded that similar to the activity toward the ORR, the activity of Co_3O_4 nanoplates toward the OER decreases with an increase of the calcination temperature. From a recent report [50], the factors for the OER activity in $Co(OH)_2$ and Co_3O_4 catalysts include surface area, electrochemical surface area, surface lattice planes, and oxidation state. In our study, Co_3O_4 calcined at 200 °C has a higher BET surface area than $Co(OH)_2$, but the OER activity is lower. To elucidate the reason, we examined the electrochemical surface area by determining the

double-layer capacitance (C_{DL}) formed at the electrode/electrolyte interface (Figure S8). The C_{DL} values for $Co(OH)_2$ and Co_3O_4 are 21.2 and 14.5 mF cm^{-2}, respectively. Thus, the higher electrochemical surface area may be responsible for the higher OER activity of $Co(OH)_2$. Actually, the similar behavior has been reported in Lee's work, in which the specific surface area of Co_3O_4 nanoplates is higher than that of $Co(OH)_2$ due to the nanopore formation after heat treatment, but the OER activity is lower [32]. Another explanation is that the OER activity of metal hydr(oxy)oxide is dependent on the bond strength of M−OH, which should be neither too strong nor too weak [51]. Since the oxygen electrocatalysis on metal oxides begins with protonation of the surface metal centers to form M−OH, the higher OER activity of $Co(OH)_2$ than Co_3O_4 can possibly be due to the removal of a kinetic step in the overall scheme of reactions [28]. However, Co_3O_4 can be reversibly converted to CoO_2, while $Co(OH)_2$ nanoparticle can form CoOOH species with a negligible conversion to CoO_2 species [50]. In addition, Zhong et al. found that the first LSV curve of $Co(OH)_2$ has a larger anodic peak than the following cycles, indicating the irreversible oxidation of $Co(OH)_2$ to CoOOH, which is further confirmed by XRD and Raman analyses [33]. Thus, $Co(OH)_2$ suffers from poor stability in the electrochemical charge-transfer reactions. For Co_3O_4 nanoplates calcined at 200 ^oC, we measured the OER stability through maintaining the current density of 10 mA cm^{-2} for 5 h, from which the overpotential increases 0.041 V (Figure S9a). After the test, the hexagonal nanoplate morphology is also preserved (Figure S9b), showing the good OER stability.

3.3 Pseudocapacitive behavior

As shown in the inset of Figure 5d, a small peak appears prior to the OER process, which is correlated to the pseudocapacitive behaviors. The CV curves of $Co(OH)_2$ and Co_3O_4 nanoplates in the potential range of 0.2 to 0.7 V (vs. Hg/HgO) at various scan rates are displayed in Figure

S10, and their comparisons at the scan rate of 40 mV s^{-1} are shown in Figure 6a. The shapes are non-rectangular, which reveals the reversible redox reactions, and the anodic (positive current density) and cathodic (negative current density) peaks represent the oxidation and reduction processes, respectively. Previous work has illustrated that cobalt oxides can undergo electrochemical charge-transfer reactions of $Co^{2+} \leftrightarrow Co^{3+} \leftrightarrow Co^{4+}$ in alkaline solutions [34,35]:

$$3Co(OH)_2 + 2OH^- \longleftrightarrow Co_3O_4 + 4H_2O + 2e^- \quad (I)$$

$$Co_3O_4 + OH^- + H_2O \longleftrightarrow 3CoOOH + e^- \quad (II)$$

$$CoOOH + OH^- \longleftrightarrow CoO_2 + H_2O + e^- \quad (III)$$

which involve the redox couples of $Co_3O_4/Co(OH)_2$, Co_3O_4/CoOOH, and CoOOH/CoO_2. Here, the peaks corresponding to each redox couple are not obvious, and instead, only one couple of peaks is presented. The similar phenomena have also been reported [39,52], which may be caused by surface modification and/or different alkaline concentrations [53,54]. The CV shapes of Co_3O_4 nanoplates calcined at different temperatures are similar, but the current density of the peak remarkably decreases with an increase of the calcination temperature. In addition, $Co(OH)_2$ nanoplates exhibit a different CV shape, which may be caused by the introduction of Reaction I. For $Co(OH)_2$ and Co_3O_4 nanoplates, the anodic scans of CV curves are not entirely symmetric with the corresponding cathodic scans, indicating that the redox process is kinetically irreversibility owing to the polarization and ohmic resistance [55–57]. When the scan rate increases, the currents increase accordingly in all samples, and the shapes are well maintained (Figure S11), indicating the good rate capability. For $Co(OH)_2$ nanoplates, the capacitance value is calculated to be 416 F g^{-1} at 10 mV s^{-1} and decreases to 339 F g^{-1} at 100 mV s^{-1}. For Co_3O_4 nanoplates calcined at 200 °C, the capacitance value is 526 F g^{-1} at 10 mV s^{-1}, higher than that of the $Co(OH)_2$ nanoplates. However, when the calcination temperature increases from 250 to 750

°C, the capacitance values of Co_3O_4 nanoplates dramatically decrease (Figure 6b), which are 298, 151, 80, and 37 F g^{-1}, respectively (Table 1). Thus, for Co_3O_4 nanoplates calcined at the temperature higher than 350 °C, the capacitance is almost negligible. For reported Co_3O_4-based catalysts used for the ORR and OER, the calcination temperatures are generally higher than 350 °C [27,29]. Consequently, good performance toward ORR and OER but no pseudocapacitive behaviors is presented in most reported Zn-air batteries [27,29,58–61].

3.4 Performance comparisons

To investigate the mechanism of electrochemical property changes of Co_3O_4 nanoplates calcined at different temperatures, we calculated the current densities in the ORR (at 0.3 V vs. RHE) and OER (at 1.65 V vs. RHE) and the capacitance based on the BET [62] and electrochemical surface areas [33]. As listed in Table 2, when the calcination temperature increases, the resultant normalized current density based on the BET areas in the ORR process exhibits an increase firstly till the calcination temperature reaches 550 °C, and then starts to decrease. This phenomenon may be explained as follows: although the current density decreases with the calcination temperature, the specific surface area decreases as well. Consequently, the normalized current density reaches the maximum value at a high temperature. When based on the electrochemical surface area (C_{DL}), interestingly, the normalized current density keeps increasing with an increase of the calcination temperature. The similar behaviors can be observed in the OER performance, in which the normalized current density based on the BET area decreases with an increase of the calcination temperature, but the value based on the electrochemical surface area shows a reversed trend. However, for the normalized capacitance, no matter based on the BET or electrochemical surface areas, the sample calcined at the lowest temperature demonstrates the largest value.

To elucidate the possible determining factor for the oxygen electrocatalysis and pseudocapacitive performance, the surface oxidation states and electronic structure of Co_3O_4 nanoplates calcined at different temperatures are further analyzed using XPS. Figure 7a shows the spectra of O 1s, which can be decomposed into three components, including the superoxide ions (531.8 eV), peroxide ions (530.6 eV), and lattice oxygen (529.5 eV) [63]. The percentage of adsorbed oxygen species (O_2^-, O^-) and lattice oxygen (O_{lat}) are listed in Table S3, and their ratios are listed in Table 2. The percentages of lattice oxygen in all samples are around 60%, but for the samples calcined at higher temperatures (500 and 750 °C), the values are smaller. This may be caused by the increase of oxygen vacancies due to the high calcination temperature [64]. Figure 7b shows the spectra of Co 2p, in which the peaks located at around 781.2 eV and 796.5 eV are attributable to Co^{2+}, and the peaks at 794.7 eV and 779.8 eV are assigned to Co^{3+} [65–67]. As the oxidation state of Co is reported to be a determining factor of the activity [63], we calculated the surface atomic ratios of Co^{2+}/Co^{3+} in Co_3O_4 nanoplates calcined at different temperatures based on the fitted curves of Co $2p_{3/2}$ peak. As listed in Table 2, the largest Co^{2+}/Co^{3+} ratio is found for the Co_3O_4 nanoplates calcined at 200 °C, and the ratio decreases with an increase of the calcination temperature, suggesting that the low-temperature calcination is beneficial for the formation of Co^{2+} [68]. From the XPS results, the high calcination temperature leads to the high amounts of adsorbed oxygen species and Co^{3+} atoms on the surface, which may be the key for the high intrinsic ORR and OER activity based on the electrochemical surface area [69,70]. However, the apparent performance is insufficient due to the greatly reduced surface area. For the pseudocapacitive performance, on the contrary, the greater amount of Co^{2+} on the surface is favorable. Considering the apparent overall activity, the low-temperature calcination of Co_3O_4 is found to be an effective method to enhance the electrochemical performance.

5. Conclusions

In this study, we have explored the electrochemical performance of Co_3O_4 in alkaline solutions to explain the reported inconsistent results. Co_3O_4 nanoplates are fabricated from $Co(OH)_2$ nanoplates using different calcination temperatures, and their morphologies, microstructures, and electrochemical behaviors in alkaline solutions are systemically characterized. The pristine $Co(OH)_2$ nanoplates have a hexagonal nanoplate morphology with the specific surface area of 61.65 $m^2\ g^{-1}$. When converted to Co_3O_4 nanoplates, the specific surface areas decrease from 101.15 to 71.72 $m^2\ g^{-1}$ when the calcination temperature increases from 200 to 750 ^oC, and the high calcination temperatures (> 550 ^oC) destroy the hexagonal morphology. The ORR/OER activity was examined in alkaline solutions. For the ORR activity, the limiting current density is 4.78 mA cm^{-2} for the $Co(OH)_2$ nanoplates, and changes from 5.32 to 4.32 for the Co_3O_4 nanoplates calcined at the temperature from 200 to 750 ^oC. Hence, the ORR activity of Co_3O_4 can be either higher or lower than that of $Co(OH)_2$, which depends on the calcination temperature. For the OER activity, at the current density of 10 mA cm^{-2}, $Co(OH)_2$ nanoplates exhibit an overpotential of 366.8 mV, while the overpotential of Co_3O_4 nanoplates increases from 390.1 to 425.7 mV when the calcination temperature increases from 200 to 750 ^oC. Hence, similar to the ORR activity, the OER activity of Co_3O_4 nanoplates decreases with an increase of the calcination temperature. Moreover, the capacitance value of Co_3O_4 nanoplates calcined at 200 ^oC reaches 526 F g^{-1}, but dramatically decreases with the calcination temperature, and becomes almost negligible when calcined at the temperature higher than 350 ^oC. From the ORR/OER activity based on the BET and electrochemical surface areas, we found that the resultant normalized current density based on the BET areas in the ORR process exhibits an increase firstly till the calcination temperature reaches 550 ^oC, and then starts to decrease. When

based on the electrochemical surface area, the normalized current density keeps increasing with an increase of the calcination temperature. The similar behaviors can be observed in the OER performance, in which the normalized current density based on the BET area decreases with an increase of the calcination temperature, but the value based on the electrochemical surface area shows a reversed trend. However, for the normalized capacitance, no matter based on the BET or electrochemical surface areas, the sample calcined at the lowest temperature demonstrates the largest value. From the XPS results, the high calcination temperature leads to the high amounts of adsorbed oxygen species and Co^{3+} atoms on the surface, which may be the key for the high intrinsic ORR and OER activity based on the electrochemical surface area. For the pseudocapacitive performance, on the contrary, the greater amount of Co^{2+} on the surface is favorable. Hence, the inconsistent electrochemical performance of Co_3O_4 may originate from different geometries and oxidation states on the surface, which are affected by the calcination temperatures in the synthesis process. Considering the apparent overall activity, the low-temperature calcination of Co_3O_4 is found to be an effective method to enhance the electrochemical performance. This work provides insights into the design and optimization of non-precious materials in electrochemical systems, and offers a feasible strategy to improve the performance by using low-temperature calcination.

Acknowledgments

P. Tan thanks the funding support from CAS Pioneer Hundred Talents Program. Z. Wu thanks the funding support from Hong Kong Scholar Program (XJ2017023) and the National Natural Science Foundation of China (51506174). M. Ni thanks the funding support from The Hong Kong Polytechnic University (G-YBJN and G-YW2D), a fund from RISUD (1-ZVEA),

and a grant (Project Number: PolyU 152214/17E) from Research Grant Council, University Grants Committee, Hong Kong SAR.

References

[1] Z.P. Cano, D. Banham, S. Ye, A. Hintennach, J. Lu, M. Fowler, Z. Chen, Batteries and fuel cells for emerging electric vehicle markets, Nat. Energy. 3 (2018) 279–289.

[2] P. Tan, H.R. Jiang, X.B. Zhu, L. An, C.Y. Jung, M.C. Wu, L. Shi, W. Shyy, T.S. Zhao, Advances and challenges in lithium-air batteries, Appl. Energy. 204 (2017) 780–806.

[3] M.A. Rahman, X. Wang, C. Wen, High Energy Density Metal-Air Batteries: A Review, J. Electrochem. Soc. 160 (2013) A1759–A1771.

[4] Y. Li, J. Lu, Metal–Air Batteries: Will They Be the Future Electrochemical Energy Storage Device of Choice?, ACS Energy Lett. 2 (2017) 1370–1377.

[5] R. Schmuch, R. Wagner, G. Hörpel, T. Placke, M. Winter, Performance and cost of materials for lithium-based rechargeable automotive batteries, Nat. Energy. 3 (2018) 267–278.

[6] P. Tan, B. Chen, H. Xu, H. Zhang, W. Cai, M. Ni, M. Liu, Z. Shao, Flexible Zn– and Li–air batteries: recent advances, challenges, and future perspectives, Energy Environ. Sci. 10 (2017) 2056–2080.

[7] J. Fu, Z.P. Cano, M.G. Park, A. Yu, M. Fowler, Z. Chen, Electrically Rechargeable Zinc-Air Batteries: Progress, Challenges, and Perspectives, Adv. Mater. 29 (2017) 1604685.

[8] P. Tan, Z. Wei, W. Shyy, T.S. Zhao, Prediction of the theoretical capacity of non-aqueous lithium-air batteries, Appl. Energy. 109 (2013) 275–282.

[9] D. Geng, N. Ding, T.S.A. Hor, S.W. Chien, Z. Liu, D. Wuu, X. Sun, Y. Zong, From Lithium-Oxygen to Lithium-Air Batteries: Challenges and Opportunities, Adv. Energy

Mater. 6 (2016) 1502164.

[10] Y. Li, H. Dai, Recent advances in zinc–air batteries, Chem. Soc. Rev. 43 (2014) 5257–5275.

[11] Z.-L. Wang, D. Xu, J.-J. Xu, X.-B. Zhang, Oxygen electrocatalysts in metal-air batteries: from aqueous to nonaqueous electrolytes, Chem. Soc. Rev. 43 (2014) 7746–7786.

[12] P. Tan, M. Liu, Z. Shao, M. Ni, Recent Advances in Perovskite Oxides as Electrode Materials for Nonaqueous Lithium-Oxygen Batteries, Adv. Energy Mater. 7 (2017) 1602674.

[13] K.-N. Jung, J. Kim, Y. Yamauchi, M.-S. Park, J.-W. Lee, J.H. Kim, Rechargeable lithium–air batteries: a perspective on the development of oxygen electrodes, J. Mater. Chem. A. 4 (2016) 14050–14068.

[14] X. Chen, C. Zhong, B. Liu, Z. Liu, X. Bi, N. Zhao, X. Han, Y. Deng, J. Lu, W. Hu, Atomic Layer Co_3O_4 Nanosheets: The Key to Knittable Zn-Air Batteries, Small. 1702987 (2018) 1702987.

[15] P. Tan, B. Chen, H. Xu, W. Cai, M. Liu, Z. Shao, M. Ni, Nanoporous NiO/$Ni(OH)_2$ Plates Incorporated with Carbon Nanotubes as Active Materials of Rechargeable Hybrid Zinc Batteries for Improved Energy Efficiency and High-Rate Capability, J. Electrochem. Soc. 165 (2018) A2119–A2126.

[16] H. Cheng, K. Scott, Selection of oxygen reduction catalysts for rechargeable lithium-air batteries-Metal or oxide?, Appl. Catal. B Environ. 108–109 (2011) 140–151.

[17] X. Ren, X. Ji, Y. Wei, D. Wu, Y. Zhang, M. Ma, Z. Liu, A.M. Asiri, Q. Wei, X. Sun, In situ electrochemical development of copper oxide nanocatalysts within a TCNQ nanowire array: A highly conductive electrocatalyst for the oxygen evolution reaction, Chem.

Commun. 54 (2018) 1425–1428.

[18] D. Fan, X. Sun, D. Wu, J. Zhao, Q. Han, Q. Wei, X. Kuang, X. Ren, Ultra-thin wrinkled NiOOH-NiCr2O4 nanosheets on Ni foam: an advanced catalytic electrode for oxygen evolution reaction, Chem. Commun. 1 (2018) 4987–4990.

[19] Y.P. Deng, Y. Jiang, D. Luo, J. Fu, R. Liang, S. Cheng, Z. Bai, Y. Liu, W. Lei, L. Yang, J. Zhu, Z. Chen, Hierarchical Porous Double-Shelled Electrocatalyst with Tailored Lattice Alkalinity toward Bifunctional Oxygen Reactions for Metal-Air Batteries, ACS Energy Lett. 2 (2017) 2706–2712.

[20] J. Liu, L. Jiang, Q. Tang, E. Wang, L. Qi, S. Wang, G. Sun, Amide-functionalized carbon supports for cobalt oxide toward oxygen reduction reaction in Zn-air battery, Appl. Catal. B Environ. 148–149 (2014) 212–220.

[21] D. Wu, Y. Wei, X. Ren, X. Ji, Y. Liu, X. Guo, Z. Liu, A.M. Asiri, Q. Wei, X. Sun, $Co(OH)_2$ Nanoparticle-Encapsulating Conductive Nanowires Array: Room-Temperature Electrochemical Preparation for High-Performance Water Oxidation Electrocatalysis, Adv. Mater. 30 (2018) 1705366.

[22] Y. Zhang, X. Ren, H. Ju, H. Ma, X. Kuang, Q. Wei, T. Yan, Y. Wei, D. Wu, X. Sun, $CoC_2O_4{\cdot}2H_2O$ derived Co_3O_4 nanorods array: a high-efficiency 1D electrocatalyst for alkaline oxygen evolution reaction , Chem. Commun. 54 (2018) 1533–1536.

[23] Q. Wei, D. Liu, B. Du, R. Ge, X. Ren, Y. Zhang, D. Wu, X. Sun, Cobalt–borate nanowire array as a high-performance catalyst for oxygen evolution reaction in near-neutral media, J. Mater. Chem. A. 5 (2017) 7291–7294.

[24] T. Li, Y. Lu, S. Zhao, Z. Gao, Y.-Y. Song, Co_3O_4-doped Co/CoFe nanoparticles encapsulated in carbon shells as bifunctional electrocatalysts for rechargeable Zn–Air

batteries, J. Mater. Chem. A. 6 (2018) 3730–3737.

[25] X. Ren, D. Wu, R. Ge, X. Sun, H. Ma, T. Yan, Y. Zhang, B. Du, Q. Wei, L. Chen, Self-supported $CoMoS_4$ nanosheet array as an efficient catalyst for hydrogen evolution reaction at neutral pH, Nano Res. 11 (2018) 2024–2033.

[26] J. Zhao, X. Ren, H. Ma, X. Sun, Y. Zhang, T. Yan, Q. Wei, D. Wu, Synthesis of Self-Supported Amorphous $CoMoO_4$ Nanowire Array for Highly Efficient Hydrogen Evolution Reaction, ACS Sustain. Chem. Eng. 5 (2017) 10093–10098.

[27] D.U. Lee, M.G. Park, H.W. Park, M.H. Seo, X. Wang, Z. Chen, Highly Active and Durable Nanocrystal-Decorated Bifunctional Electrocatalyst for Rechargeable Zinc-Air Batteries, ChemSusChem. 8 (2015) 3129–3138.

[28] C. Lin, S.S. Shinde, Y. Wang, Y. Sun, S. Chen, H. Zhang, X. Li, J.-H. Lee, Flexible and rechargeable Zn–air batteries based on green feedstocks with 75% round-trip efficiency, Sustain. Energy Fuels. 1 (2017) 1909–1914.

[29] C. Guan, A. Sumboja, H. Wu, W. Ren, X. Liu, H. Zhang, Z. Liu, C. Cheng, S.J. Pennycook, J. Wang, Hollow Co_3O_4 Nanosphere Embedded in Carbon Arrays for Stable and Flexible Solid-State Zinc-Air Batteries, Adv. Mater. 29 (2017) 1704117.

[30] D. Su, S. Dou, G. Wang, Single Crystalline Co_3O_4 Nanocrystals Exposed with Different Crystal Planes for Li-O_2 Batteries, Sci. Rep. 4 (2015) 5767.

[31] X. Zhou, Z. Xia, Z. Tian, Y. Ma, Y. Qu, Ultrathin porous Co_3O_4 nanoplates as highly efficient oxygen evolution catalysts, J. Mater. Chem. A. 3 (2015) 8107–8114.

[32] Y. Zhan, G. Du, S. Yang, C. Xu, M. Lu, Z. Liu, J.Y. Lee, Development of Cobalt Hydroxide as a Bifunctional Catalyst for Oxygen Electrocatalysis in Alkaline Solution, ACS Appl. Mater. Interfaces. 7 (2015) 12930–12936.

[33] Z. Song, X. Han, Y. Deng, N. Zhao, W. Hu, C. Zhong, Clarifying the Controversial Catalytic Performance of $Co(OH)_2$ and Co_3O_4 for Oxygen Reduction/Evolution Reactions toward Efficient Zn-Air Batteries, ACS Appl. Mater. Interfaces. 9 (2017) 22694–22703.

[34] I.G. Casella, M. Gatta, Study of the electrochemical deposition and properties of cobalt oxide species in citrate alkaline solutions, J. Electroanal. Chem. 534 (2002) 31–38.

[35] P. Nkeng, Characterization of Spinel-Type Cobalt and Nickel Oxide Thin Films by X-Ray Near Grazing Diffraction, Transmission and Reflectance Spectroscopies, and Cyclic Voltammetry, J. Electrochem. Soc. 142 (1995) 1777–1783.

[36] X. Wang, F. Wang, L. Wang, M. Li, Y. Wang, B. Chen, Y. Zhu, L. Fu, L. Zha, L. Zhang, Y. Wu, W. Huang, An Aqueous Rechargeable Zn//Co_3O_4 Battery with High Energy Density and Good Cycling Behavior, Adv. Mater. 28 (2016) 4904–4911.

[37] P. Tan, B. Chen, H. Xu, W. Cai, W. He, M. Liu, Z. Shao, M. Ni, Co_3O_4 Nanosheets as Active Material for Hybrid Zn Batteries, Small. 14 (2018) 1800225.

[38] P. Tan, B. Chen, H. Xu, W. Cai, W. He, M. Ni, Investigation on the electrode design of hybrid Zn-Co_3O_4/air batteries for performance improvements, Electrochim. Acta. 283 (2018) 1028–1036.

[39] P. Tan, B. Chen, H. Xu, W. Cai, W. He, M. Ni, In-situ growth of Co_3O_4 nanowire-assembled clusters on nickel foam for aqueous rechargeable Zn-Co_3O_4 and Zn-air batteries, Appl. Catal. B Environ. 241 (2019) 104–112.

[40] D.U. Lee, J.-Y. Choi, K. Feng, H.W. Park, Z. Chen, Advanced Extremely Durable 3D Bifunctional Air Electrodes for Rechargeable Zinc-Air Batteries, Adv. Energy Mater. 4 (2014) 1301389.

[41] P. Tan, B. Chen, H. Xu, W. Cai, W. He, M. Ni, Porous Co_3O_4 nanoplates as the active

material for rechargeable Zn-air batteries with high energy efficiency and cycling stability, Energy. 166 (2019) 1241–1248.

[42] X. Zhou, Z. Xia, Z. Tian, Y. Ma, Y. Qu, Ultrathin porous Co_3O_4 nanoplates as highly efficient oxygen evolution catalysts, J. Mater. Chem. A. 3 (2015) 8107–8114.

[43] W. Gou, X. Zhou, J. Li, Y. Ma, Nanoporous Co_3O_4 plates as highly electroactive materials for electrochemical energy storage, Mater. Lett. 180 (2016) 207–211.

[44] R.R. Salunkhe, J. Lin, V. Malgras, S.X. Dou, J.H. Kim, Y. Yamauchi, Large-scale synthesis of coaxial carbon nanotube/$Ni(OH)_2$ composites for asymmetric supercapacitor application, Nano Energy. 11 (2015) 211–218.

[45] F. Meng, H. Zhong, D. Bao, J. Yan, X. Zhang, In Situ Coupling of Strung Co_4N and Intertwined N–C Fibers toward Free-Standing Bifunctional Cathode for Robust, Efficient, and Flexible Zn–Air Batteries, J. Am. Chem. Soc. 138 (2016) 10226–10231.

[46] Z. Liu, R. Ma, M. Osada, K. Takada, T. Sasaki, Selective and controlled synthesis of α- and β-cobalt hydroxides in highly developed hexagonal platelets, J. Am. Chem. Soc. 127 (2005) 13869–13874.

[47] D. Ghosh, S. Giri, C.K. Das, Hydrothermal synthesis of platelet β-$Co(OH)_2$ and Co_3O_4 : Smart electrode material for energy storage application, Environ. Prog. Sustain. Energy. 33 (2014) 1059–1064.

[48] J.-H. Zhong, A.-L. Wang, G.-R. Li, J.-W. Wang, Y.-N. Ou, Y.-X. Tong, Co_3O_4/$Ni(OH)_2$ composite mesoporous nanosheet networks as a promising electrode for supercapacitor applications, J. Mater. Chem. 22 (2012) 5656.

[49] X. Liu, R. Yi, N. Zhang, R. Shi, X. Li, G. Qiu, Cobalt hydroxide nanosheets and their thermal decomposition to cobalt oxide nanorings, Chem. - An Asian J. 3 (2008) 732–738.

[50] S. Gupta, A. Yadav, S. Bhartiya, M.K. Singh, A. Miotello, A. Sarkar, N. Patel, Co oxide nanostructures for electrocatalytic water-oxidation: Effects of dimensionality and related properties, Nanoscale. 10 (2018) 8806–8819.

[51] R. Subbaraman, D. Tripkovic, K.-C. Chang, D. Strmcnik, A.P. Paulikas, P. Hirunsit, M. Chan, J. Greeley, V. Stamenkovic, N.M. Markovic, Trends in activity for the water electrolyser reactions on 3d M(Ni,Co,Fe,Mn) hydr(oxy)oxide catalysts, Nat. Mater. 11 (2012) 550.

[52] P. Bhojane, L. Sinha, R.S. Devan, P.M. Shirage, Mesoporous layered hexagonal platelets of Co_3O_4 nanoparticles with (111) facets for battery applications: high performance and ultra-high rate capability, Nanoscale. 10 (2018) 1779–1787.

[53] E.B. Castro, C.A. Gervasi, J.R. Vilche, Oxygen evolution on electrodeposited cobalt oxides, J. Appl. Electrochem. 28 (1998) 835–841.

[54] S.K. Meher, G.R. Rao, Effect of microwave on the nanowire morphology, optical, magnetic, and pseudocapacitance behavior of Co_3O_4, J. Phys. Chem. C. 115 (2011) 25543–25556.

[55] S.K. Meher, P. Justin, G. Ranga Rao, Microwave-Mediated Synthesis for Improved Morphology and Pseudocapacitance Performance of Nickel Oxide, ACS Appl. Mater. Interfaces. 3 (2011) 2063–2073.

[56] W.G. Pell, B.E. Conway, Voltammetry at a de Levie brush electrode as a model for electrochemical supercapacitor behaviour, J. Electroanal. Chem. 500 (2001) 121–133.

[57] S.K. Meher, P. Justin, G. Ranga Rao, Nanoscale morphology dependent pseudocapacitance of NiO: Influence of intercalating anions during synthesis, Nanoscale. 3 (2011) 683–692.

[58] J. Fu, F.M. Hassan, J. Li, D.U. Lee, A.R. Ghannoum, G. Lui, M.A. Hoque, Z. Chen, Flexible Rechargeable Zinc-Air Batteries through Morphological Emulation of Human Hair Array, Adv. Mater. 28 (2016) 6421–6428.

[59] B. Li, X. Ge, F.W.T. Goh, T.S.A. Hor, D. Geng, G. Du, Z. Liu, J. Zhang, X. Liu, Y. Zong, Co_3O_4 nanoparticles decorated carbon nanofiber mat as binder-free air-cathode for high performance rechargeable zinc-air batteries, Nanoscale. 7 (2015) 1830–1838.

[60] S. Zeng, H. Chen, H. Wang, X. Tong, M. Chen, J. Di, Q. Li, Crosslinked Carbon Nanotube Aerogel Films Decorated with Cobalt Oxides for Flexible Rechargeable Zn-Air Batteries, Small. 13 (2017) 1700518.

[61] G. Du, X. Liu, Y. Zong, T.S.A. Hor, A. Yu, Z. Liu, Co_3O_4 nanoparticle-modified MnO_2 nanotube bifunctional oxygen cathode catalysts for rechargeable zinc–air batteries, Nanoscale. 5 (2013) 4657–4661.

[62] J.T. Mefford, X. Rong, A.M. Abakumov, W.G. Hardin, S. Dai, A.M. Kolpak, K.P. Johnston, K.J. Stevenson, Water electrolysis on $La_{1-x}Sr_xCoO_{3-\delta}$ perovskite electrocatalysts, Nat. Commun. 7 (2016) 11053.

[63] Y. Sun, J. Liu, J. Song, S. Huang, N. Yang, J. Zhang, Y. Sun, Y. Zhu, Exploring the Effect of Co_3O_4 Nanocatalysts with Different Dimensional Architectures on Methane Combustion, ChemCatChem. 8 (2016) 540–545.

[64] D. Chen, C. Chen, Z.M. Baiyee, Z. Shao, F. Ciucci, Nonstoichiometric Oxides as Low-Cost and Highly-Efficient Oxygen Reduction/Evolution Catalysts for Low-Temperature Electrochemical Devices, Chem. Rev. 115 (2015) 9869–9921.

[65] J. Guan, L. Bai, M. Li, X. Yang, X. Wen, Co/CoO_x nanoparticles inlaid onto nitrogen-doped carbon-graphene as a trifunctional electrocatalyst, Electrochim. Acta. 296 (2018)

830–841.

[66] M. Li, L. Bai, S. Wu, X. Wen, J. Guan, Co/CoO_x Nanoparticles Embedded on Carbon for Efficient Catalysis of Oxygen Evolution and Oxygen Reduction Reactions, ChemSusChem. 11 (2018) 1722–1727.

[67] J. Guan, C. Ding, R. Chen, B. Huang, X. Zhang, F. Fan, F. Zhang, C. Li, CoO_x nanoparticle anchored on sulfonated-graphite as efficient water oxidation catalyst, Chem. Sci. 8 (2017) 6111–6116.

[68] K.-L. Yan, J.-F. Qin, J.-H. Lin, B. Dong, J.-Q. Chi, Z.-Z. Liu, F.-N. Dai, Y.-M. Chai, C.-G. Liu, Probing the active sites of Co_3O_4 for the acidic oxygen evolution reaction by modulating the Co^{2+}/Co^{3+} ratio, J. Mater. Chem. A. 6 (2018) 5678–5686.

[69] C. Wei, Z. Feng, G.G. Scherer, J. Barber, Y. Shao-Horn, Z.J. Xu, Cations in Octahedral Sites: A Descriptor for Oxygen Electrocatalysis on Transition-Metal Spinels, Adv. Mater. 29 (2017) 1–8.

[70] G. Chen, Z. Hu, Y. Zhu, Z.-G. Chen, Y. Zhong, H.-J. Lin, C.-T. Chen, L.H. Tjeng, W. Zhou, Z. Shao, Ultrahigh-performance tungsten-doped perovskites for the oxygen evolution reaction, J. Mater. Chem. A. 6 (2018) 9854–9859.

Figures

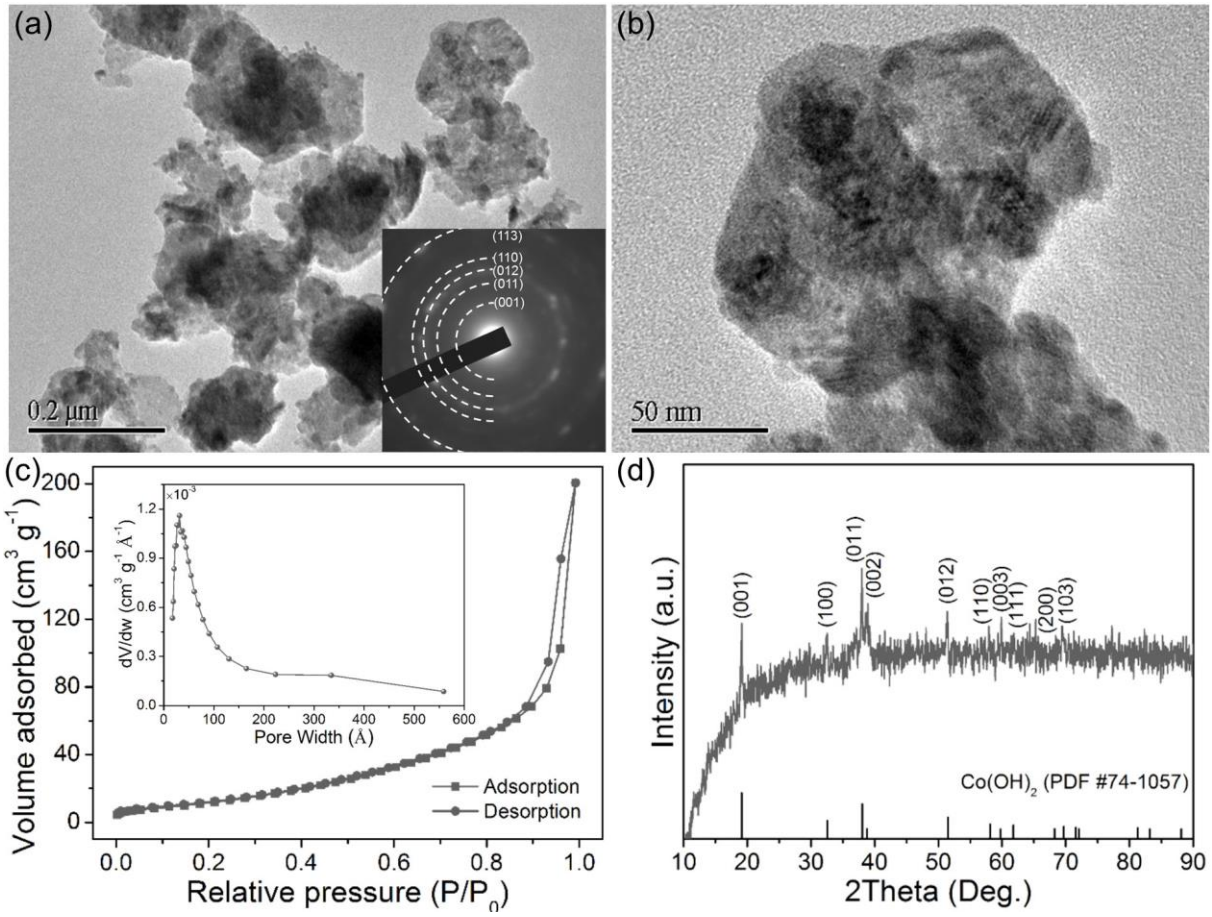

Figure 1. Characterization of $Co(OH)_2$ nanoplates. (a) TEM image, the inset shows the SAED. (b) High-magnification TEM image. (c) Nitrogen adsorption-desorption isotherms, and the inest shows the pore size distribution. (d) XRD pattern.

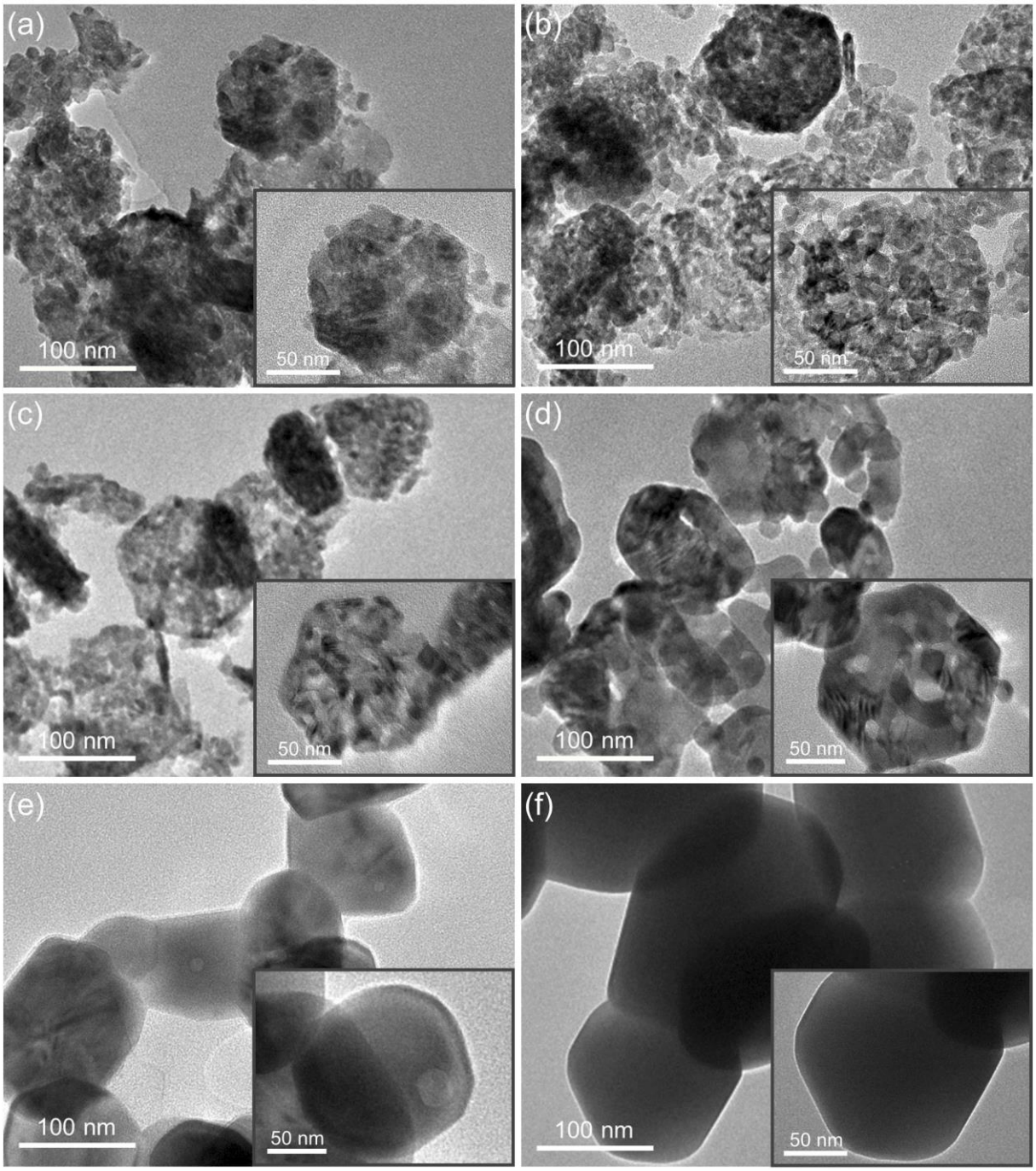

Figure 2. TEM images of the nanoplates calcined at different temperatures, and the insets show the TEM images with a high magnification: (a) 150 ^{o}C, (b) 200 ^{o}C, (c) 250 ^{o}C, (d) 350 ^{o}C, (e) 550 ^{o}C, and (f) 750 ^{o}C.

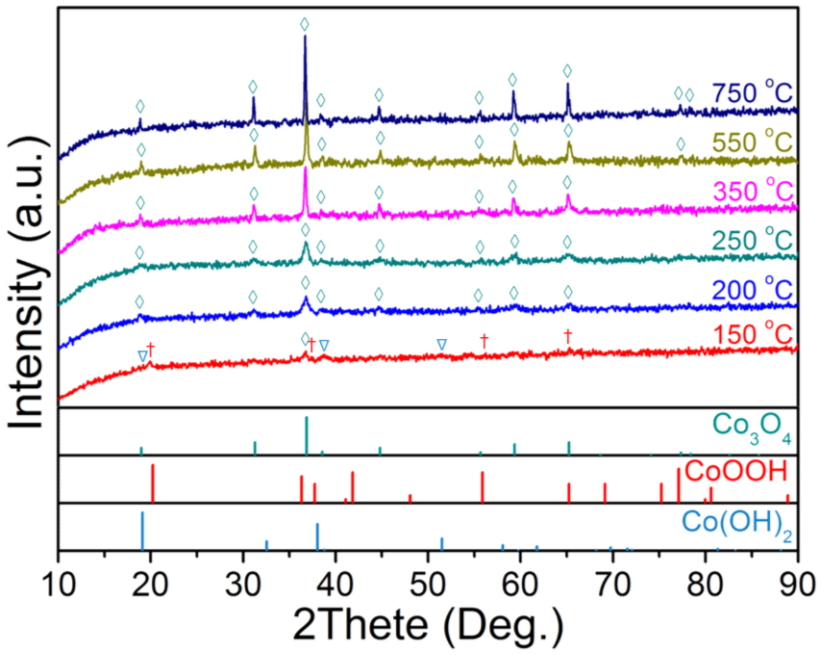

Figure 3. XRD patterns of the nanoplates calcined at different temperatures.

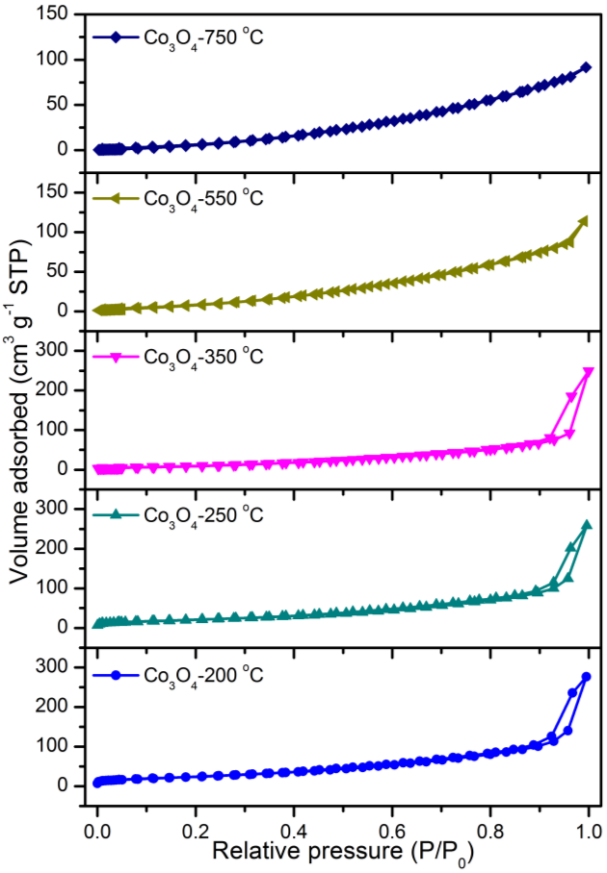

Figure 4. Nitrogen adsorption-desorption isotherms of Co_3O_4 nanoplates calcined at different temperatures.

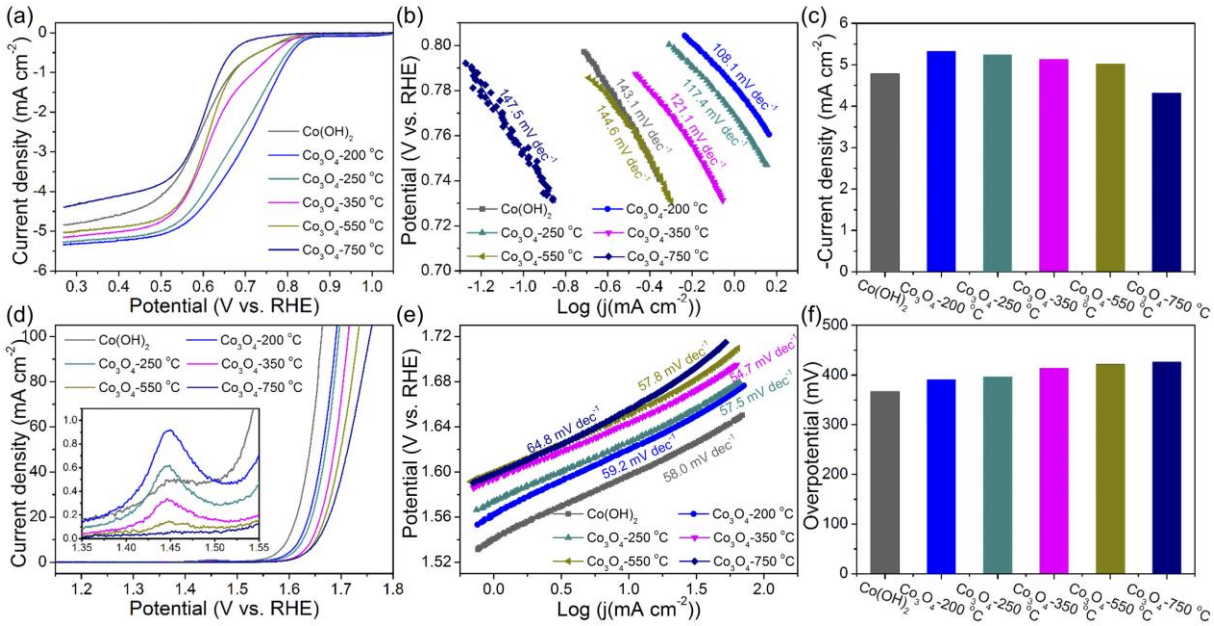

Figure 5. The electrochemical activity of $Co(OH)_2$ and Co_3O_4 nanoplates for oxygen electrocatalysis. (a) LSV curves for ORR the polarization in the O_2 saturated 0.1 M KOH solution at a scan rate of 5 mV s^{-1} and a rotation speed of 1600 rpm. (b) Tafel plots for the ORR polarization. (c) Limiting current densities (0.3 V vs. RHE) (d) LSV curves for the OER polarization in 1.0 M KOH solution at a scan rate of 5 mV s^{-1}. (e) Tafel plots for the OER polarization. (f) Overpotential at the current density of 10 mA cm^{-2}.

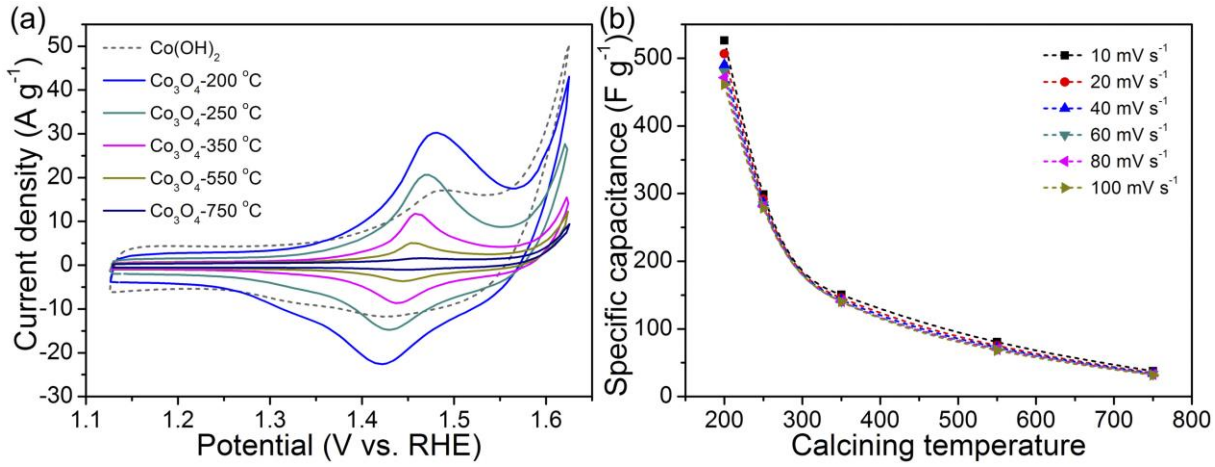

Figure 6. Pseudocapacitive behaviors in 1.0 M KOH at a scan rate of 40 mV s^{-1}. (b) The specific capacitance of Co_3O_4 nanoplates calcined at different temperatures.

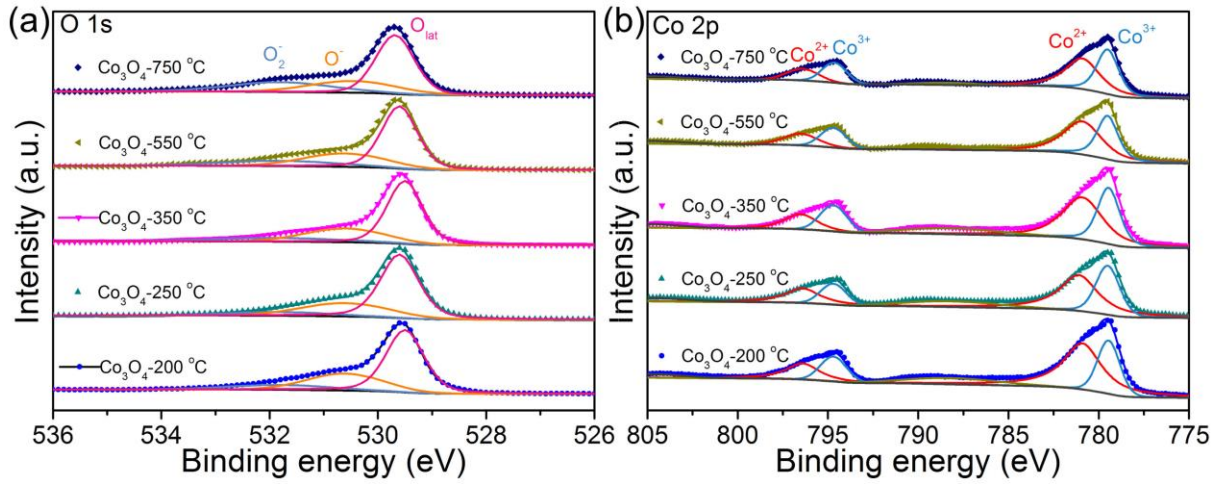

Figure 7. XPS spectra of (a) O 1s and (b) Co 2p of Co_3O_4 nanoplates calcined at different temperatures.

Tables

Table 1. Summary of geometric properties and electrochemical properties of Co_3O_4 nanoplates calcined at different temperatures

Calcination temperature (°C)	Specific surface area (m^2 g^{-1})	Pore volume (cm^3 g^{-1})	Electrochemical surface area (C_{DL}, mF cm^{-2})	Limiting current density in the ORR (at 0.3 V vs. RHE, −mA cm^{-2})	Overpotential at 10 mA cm^{-2} in the OER (mV)	Specific capacitance at 10 mV s^{-1} (F g^{-1})
200	101.15	0.409	14.5	5.32	390.1	526.3
250	90.25	0.378	8.2	5.24	396.0	298.7
350	83.71	0.353	3.9	5.13	413.2	150.6
550	76.01	0.177	2.9	5.01	421.0	80.6
750	71.72	0.141	2.0	4.32	425.7	37.4

Table 2. Summary of normalized electrochemical properties and surface oxidation states of Co_3O_4 nanoplates calcined at different temperatures

Calcination temperature (°C)	Normalized current density at 0.3 V vs. RHE		Normalized current density at 1.65 V vs. RHE		Normalized capacitance at 10 mV s^{-1} ($F\ m^{-2}$)		Ratio of Co^{2+}/Co^{3+}	Ratio of O_{lat}/O_{ad}
	Based on BET area ($-A\ m^{-2}$)	Based on C_{DL} ($-mA\ mF^{-1}$)	Based on BET area ($A\ m^{-2}$)	Based on C_{DL} ($-mA\ mF^{-1}$)	Based on BET area ($F\ m^{-2}$)	Based on C_{DL}		
200	0.26	0.37	1.61	2.27	5.20	3.63	2.12	1.53
250	0.29	0.64	1.44	3.17	3.31	3.64	1.58	1.59
350	0.31	1.32	0.79	3.34	1.80	3.86	1.56	1.80
550	0.33	1.73	0.64	3.35	1.06	2.78	1.48	1.28
750	0.30	2.16	0.58	4.18	0.52	1.87	1.24	1.18